INTERNATIONAL JOURNAL FOR NUMERICAL METHODS IN FLUIDS
Int. J. Numer. Meth. Fluids 2007; **53**:1613–1628
Published online 10 October 2006 in Wiley InterScience (www.interscience.wiley.com). DOI: 10.1002/fld.1366

A high-order accurate method for two-dimensional incompressible viscous flows

Arnab Kumar De[‡] and Vinayak Eswaran[*, †]

Department of Mechanical Engineering, Indian Institute of Technology Kanpur, India

SUMMARY

A high-order accurate solution method for complex geometries is developed for two-dimensional flows using the stream function–vorticity formulation. High-order accurate spectrally optimized compact schemes along with appropriate boundary schemes are used for spatial discretization while a two-level backward Euler implicit scheme is used for the time integration. The linear system of equations for stream function and vorticity are solved by an inner iteration while contravariant velocities constitute outer iterations. The effect of curvilinear grids on the solution accuracy is studied. The method is used to compute Cartesian and inclined driven cavity, flow in a triangular cavity and viscous flow in constricted channel. Benchmark-like accuracy is obtained in all the problems with fewer grid points compared to reported studies. Copyright © 2006 John Wiley & Sons, Ltd.

Received 11 April 2006; Revised 3 August 2006; Accepted 6 August 2006

KEY WORDS: stream function; vorticity; compact schemes; accuracy; resolution

1. INTRODUCTION

Higher order solutions of Navier–Stokes equations [1–7] become essential not just for direct numerical simulation of turbulent flows but also for laminar flows in complex geometries. Accuracy and resolution are the two critical issues that determine the quality of the solutions. The spectral resolution of a scheme becomes particularly important at high Reynolds numbers.

Spectral and pseudo-spectral methods give highly accurate solutions of Navier–Stokes equations by adequately resolving the range of spatial scales typical of high Reynolds number flows. However, they are computationally intensive and are difficult to apply to complex geometries. In finite

*Correspondence to: Vinayak Eswaran, Department of Mechanical Engineering, Indian Institute of Technology Kanpur, Kanpur-208 016, India.
†E-mail: eswar@iitk.ac.in
‡E-mail: arkde@iitk.ac.in

difference methods, explicit schemes [8–11] achieve high-order accuracy at the expense of using a large stencil while compact schemes [12–16] use smaller stencils. Compact schemes can be designed to give optimum resolution along with required numerical stability.

Finite difference methods can easily be adopted to complex geometries. In order to solve the governing equations in curvilinear geometries, body-fitted grids are generated suitably and the equations are transformed to a rectangular geometry where they are solved. In the present work, we have used high-order compact schemes whose use till now has been largely limited to specific applications like aeroacoutics and problems with wave propagation.

In 2-D incompressible flows, the ψ–ω formulation is popular for its robustness and ease of implementation. This method bypasses a few difficulties such as velocity–pressure coupling and prescription of the pressure boundary conditions of the primitive approach [17, 18] and of solving an over determined system of equations of the velocity–vorticity method [19]. In the present paper we have attempted high-order solution of two-dimensional flows using the vorticity–stream function method. The method of solution is through false-transient time stepping. Thus, although only steady-state solutions have been obtained in this paper the method can be straightforwardly extended to unsteady problems.

The organization of the paper is the following. We start with the governing equations, the boundary conditions and their transformation. In the next section, the numerical methods adopted are described along with the solution algorithm. In Section 4, results of four benchmark problems involving rectangular as well as curvilinear geometries are presented. Finally we conclude the main findings of the work in Section 5.

2. GOVERNING EQUATIONS AND BOUNDARY CONDITIONS

The set of governing equations for the vorticity–stream function formulation includes a convection–diffusion equation for vorticity and a Poisson equation for the stream function. They are written in transformed curvilinear coordinates as

$$\omega_t + \frac{1}{J}[(U\omega)_\xi + (V\omega)_\eta] = \frac{1}{Re}\nabla^2\omega \tag{1}$$

$$\nabla^2\psi = -\omega \tag{2}$$

$$u = \frac{1}{J}(-x_\eta\psi_\xi + x_\xi\psi_\eta), \quad v = \frac{1}{J}(-y_\eta\psi_\xi + y_\xi\psi_\eta) \tag{3}$$

where $U = y_\eta u - x_\eta v$ and $V = -y_\xi u + x_\xi v$ are the contravariant velocity components in ξ and η directions, respectively. The Laplacian of a generic scalar ϕ in the transformed plane is given by

$$\nabla^2\phi = \frac{1}{J^2}(\alpha\phi_{\xi\xi} + \beta\phi_{\xi\eta} + \gamma\phi_{\eta\eta}) + \frac{1}{J^3}[(-y_\eta A + x_\eta B)\phi_\xi + (y_\xi A - x_\xi B)\phi_\eta] \tag{4}$$

where $\alpha = x_\eta^2 + y_\eta^2$, $\gamma = x_\xi^2 + y_\xi^2$, $\beta = -2(x_\xi x_\eta + y_\xi y_\eta)$, $A = \alpha x_{\xi\xi} + \beta x_{\xi\eta} + \gamma x_{\eta\eta}$ and $B = \alpha y_{\xi\xi} + \beta y_{\xi\eta} + \gamma y_{\eta\eta}$.

DOI: 10.1002/fld

2.1. Boundary conditions

The boundary conditions in the ψ–ω formulation can be prescribed primarily in two ways.

Approach 1
On the solid wall, due to no-slip conditions, the stream function takes the following conditions:

$$\psi = \text{constant} \quad \text{and} \quad \frac{\partial \psi}{\partial n} = 0 \tag{5}$$

where n denotes the normal direction to the solid wall. The constant stream function condition is applied to solve the Poisson equation for ψ while gradient condition is used along with Equation (2) to derive the condition for vorticity at the boundaries. This approach of prescribing vorticity is popular and well suited for reasonably simple geometries but has difficulties for the curvilinear geometries [20].

Approach 2
In the second approach, the stream function values at the boundaries are prescribed by a constant while vorticity is specified by its definition

$$\omega_b = \left[\frac{1}{J}(u_\xi x_\eta - u_\eta x_\xi + v_\xi y_\eta - v_\eta y_\xi) \right]_b \tag{6}$$

Although both approaches use the zero normal derivative condition (Equation (5)) for ψ, their implementation is somewhat different. The first approach leads to coupling of vorticity at the boundaries with the stream function at the inner points in each time step, while in the second approach the boundary vorticity remains decoupled from the inner point values at that particular time and only admits 'explicit update', in terms of previous time-level values. It has been found that the explicit update of the boundary vorticities in some cases enhances the numerical stability. An excellent review on vorticity boundary conditions has been given by Quartapelle *et al.* [20]. In the present work, Approach 2 has been used with higher order schemes to specify the vorticity boundary condition.

3. NUMERICAL DETAILS

In this section the numerical techniques adopted to solve the governing equations are discussed. Higher order spatial discretization of different terms are explained, and then the time integration scheme is described. Boundary conditions and the solution algorithm are also described.

3.1. Spatial discretization

Compact schemes are formed by using formulas that couple both the derivatives as well as the functional values at a point. They use a smaller stencil than explicit schemes to achieve high-order accuracy. Moreover, more number of coefficients in the compact formula facilitates optimization of the scheme in terms of spectral resolution and numerical stability.

In the present work, a sixth-order spectrally optimized central compact scheme for inner points, combined with a fourth-order central compact scheme for near boundary points and a third-order

DOI: 10.1002/fld

boundary scheme has been used for the computation of the first derivative:

$$\begin{aligned}
\sum_{j=-2}^{2} \beta_j f'_{i+j} &= \frac{1}{h} \sum_{j=-3}^{3} a_j f_{i+j}, \quad 4 \leqslant i \leqslant N-3 \\
\frac{1}{4} f'_{i-1} + f'_i + \frac{1}{4} f'_{i+1} &= \frac{1}{h} \left(-\frac{3}{4} f_{i-1} + \frac{3}{4} f_{i+1} \right), \quad i = 2, 3, N-2, N-1 \\
f'_i + 3 f'_{i-1} &= \frac{1}{h} \left(\frac{17}{6} f_i - \frac{3}{2} f_{i-1} - \frac{3}{2} f_{i-2} + \frac{1}{6} f_{i-3} \right), \quad i = N \\
f'_i + 3 f'_{i+1} &= \frac{1}{h} \left(-\frac{17}{6} f_i + \frac{3}{2} f_{i+1} + \frac{3}{2} f_{i+2} - \frac{1}{6} f_{i+3} \right), \quad i = 1
\end{aligned} \tag{7}$$

with $a_{\pm 3} = \pm 0.00559$, $a_{\pm 2} = \pm 0.25154$, $a_{\pm 1} = \pm 0.6494$, $a_0 = 0$, $\beta_{\pm 1} = 0.57967$, $\beta_{\pm 2} = 0.0895$, $\beta_0 = 1$.

For the computation of the second derivative, a fourth-order optimized compact scheme along with a third-order boundary schemes have been used:

$$\begin{aligned}
\sum_{j=-2}^{2} \alpha_j f''_{i+j} &= \frac{1}{h^2} \sum_{j=-3}^{3} b_j f_{i+j}, \quad 4 \leqslant i \leqslant N-3 \\
f''_i + \frac{1}{10}(f''_{i-1} + f''_{i+1}) &= \frac{6}{5h^2}(-f_{i-1} - 2f_i + f_{i+1}), \quad i = 2, 3, N-2, N-1 \\
f''_i + 10 f''_{i-1} &= \frac{1}{h^2} \left(\frac{145}{12} f_i - \frac{76}{3} f_{i-1} + \frac{29}{2} f_{i-2} - \frac{4}{3} f_{i-3} + \frac{1}{12} f_{i-4} \right), \quad i = N \\
f''_i + 10 f''_{i+1} &= \frac{1}{h^2} \left(\frac{145}{12} f_i - \frac{76}{3} f_{i+1} + \frac{29}{2} f_{i+2} - \frac{4}{3} f_{i+3} + \frac{1}{12} f_{i+4} \right), \quad i = 1
\end{aligned} \tag{8}$$

with $b_{\pm 1} = 0.21564935$, $b_{\pm 2} = 1.723322/4$, $b_{\pm 3} = 0.1765973/9$, $b_0 = -2(b_1 + b_2 + b_3)$, $\alpha_{\pm 1} = 0.50209266$, $\alpha_{\pm 2} = 0.05569169$, $\alpha_0 = 1$.

Equations (7) and (8) can be written in a matrix form as

$$A\mathbf{f}' = B\mathbf{f} \quad \text{and} \quad C\mathbf{f}'' = D\mathbf{f}$$

where $\mathbf{f}''$, $\mathbf{f}'$ and $\mathbf{f}$ are vectors, respectively, containing the first, second derivative and the function values along a line in a certain direction. These equations are inverted to obtain the first and second derivatives along a line in the computational plane during the solution

$$\mathbf{f}' = (A^{-1}B)\mathbf{f} \Longrightarrow \mathbf{f}' = E\mathbf{f} \quad \text{and} \quad \mathbf{f}'' = (C^{-1}D)\mathbf{f} \Longrightarrow \mathbf{f}'' = F\mathbf{f} \tag{9}$$

where $E(\equiv A^{-1}B)$ and $F(\equiv C^{-1}D)$ need to be computed only once (for each direction), during the preprocessing stage, for use in all subsequent computations. For the mixed derivatives, such as $\phi_{\xi\eta}$, arising in the diffusion term in Equations (1) and (2), successive operation by the first derivative operators of the respective directions are applied. This is written symbolically as

$$\mathbf{f}_{\xi\eta} = (\mathbf{f}_\xi)_\eta = (E_\xi \mathbf{f})_\eta = E_\eta (E_\xi \mathbf{f}) \tag{10}$$

where E_ξ and E_η are the matrix E of Equation (9) in the ξ and η directions, respectively.

DOI: 10.1002/fld

3.2. Time integration scheme

An implicit technique has been used in the present study to time march the vorticity equation (Equation (1)) which is discretized with the two-point backward Euler scheme as follows:

$$J\frac{\omega^{n+1}-\omega^{n}}{\Delta t}+U^{n+1}E_{\xi}\boldsymbol{\Omega}^{n+1}+V^{n+1}E_{\eta}\boldsymbol{\Omega}^{n+1}=\frac{1}{Re}\nabla^{2}\omega^{n+1} \tag{11}$$

where the discretized form of the Laplacian is

$$\nabla^{2}\omega=\frac{1}{J^{2}}[\alpha F_{\xi}\boldsymbol{\Omega}+\gamma F_{\xi}\boldsymbol{\Omega}+\beta F_{\eta}(F_{\xi}\boldsymbol{\Omega})]+PE_{\xi}\boldsymbol{\Omega}+QE_{\eta}\boldsymbol{\Omega} \tag{12}$$

and P and Q are same as in Equation (4). If Equation (11) is linearized by using the most-recent values of the contravariant velocities within a time step it becomes

$$J\frac{\omega^{n+1,l+1}-\omega^{n}}{\Delta t}+U^{n+1,l}E_{\xi}\boldsymbol{\Omega}^{n+1,l+1}+V^{n+1,l}E_{\eta}\boldsymbol{\Omega}^{n+1,l+1}=\frac{1}{Re}\nabla^{2}\omega^{n+1,l+1} \tag{13}$$

where l is the index for the inner-loop iteration within a time step. Equation (13), written for all the points in the computational domain, can be cast into the matrix form

$$A_{\omega}(U^{n+1,l},\,V^{n+1,l},\,g,\,Re)\omega^{n+1,l+1}=b_{\omega} \tag{14}$$

where g denotes the dependence of matrix A_{ω} on the metric coefficients and the Jacobian of the transformation. The Poisson equation for the stream function is discretized by the use of operator F of Equation (9) and the mixed derivative operator of Equation (10) to obtain a system of linear equations

$$A_{\psi}(g)\psi^{n+1,l+1}=b_{\psi}(\omega^{n+1,l+1}) \tag{15}$$

The velocity components are obtained as follows:

$$u=\frac{1}{J}[-x_{\eta}E_{\xi}\boldsymbol{\psi}^{n+1,l+1}+x_{\xi}E_{\eta}\boldsymbol{\psi}^{n+1,l+1}]\quad\text{and}\quad v=\frac{1}{J}[-y_{\eta}E_{\xi}\boldsymbol{\psi}^{n+1,l+1}+y_{\xi}E_{\eta}\boldsymbol{\psi}^{n+1,l+1}] \tag{16}$$

while the contravariant velocities are calculated using their definition

$$U^{n+1,l+1}=y_{\eta}u-x_{\eta}v\quad\text{and}\quad V^{n+1,l+1}=-y_{\xi}u+x_{\xi}v \tag{17}$$

3.3. Solution algorithm

The sequential steps that constitute the solution algorithm is written below:

1. Start with initial condition.
2. Solution is started with the values of the previous time step, $\omega^{n+1,1}=\omega^{n}$, $\psi^{n+1,1}=\psi^{n}$, $u^{n+1,1}=u^{n}$, $v^{n+1,1}=v^{n}$.
3. Solve for vorticity $\omega^{n+1,l+1}$ from Equation (14).
4. Solve for stream function $\psi^{n+1,l+1}$ from Equation (15) using $\omega^{n+1,l+1}$ of step 3.
5. Compute Cartesian and contravariant velocities using Equations (16) and (17), $\mathbf{u}^{n+1,l+1}$ and $\mathbf{U}^{n+1,l+1}$.

DOI: 10.1002/fld

6. Check for convergence of contravariant velocities. If $|\mathbf{U}^{n+1,l+1} - \mathbf{U}^{n+1,l}| > \varepsilon$, increase inner loop counter $l \leftarrow l + 1$ and repeat steps 3–4 else go to step 7.
7. March in time with $n \leftarrow n + 1$ and go to step 2.

All the systems of linear equations are solved by the stabilized Bi-conjugate gradient (BiCGStab) technique [21]. For the convergence of contravariant velocities within in a time step, the root-mean-square errors (U_{rms}, V_{rms}) are reduced to 10^{-6} where

$$U_{\text{rms}} = \sqrt{\frac{\sum\sum(U^{n+1,l+1} - U^{n+1,l})^2}{NM}}, \quad V_{\text{rms}} = \sqrt{\frac{\sum\sum(V^{n+1,l+1} - V^{n+1,l})^2}{NM}}$$

It has been seen that typically three to four inner-loop (l) iterations are required for the convergence of contravariant velocities within a time step. The convergence criteria for Equations (14) and (15) are set at 10^{-8}; it was observed that a stringent criteria for Equations (14) and (15) leads to faster convergence towards the steady-state solution.

4. RESULTS AND DISCUSSION

In this section results are presented for a number of benchmark problems and a model test case to check the accuracy achieved both for rectangular and curvilinear grids. Although the algorithm is time accurate, no attempt has been made to compute the unsteady solutions as the present work mainly focuses on high spatial accuracy.

4.1. Shear driven cavity

The lid-driven cavity problem has been solved for $Re = 100$, 400, 1000, 3200 and 5000 and compared with the benchmark results of Ghia *et al.* [22] where a multi-grid based finite-difference method was used with a finest level of grid of 129×129 for $Re \leqslant 1000$ and 256×256 for $Re = 3200$ and 5000. In the present work, the grids used are 21×21 for $Re = 100$, 31×31 for $Re = 400$, 1000 and 41×41 for $Re = 3200$, 5000. While a uniform grid has been used for $Re = 100$ and 400, a non-uniform grid with grid points more closely clustered near the walls has been used for $Re = 1000$, 3200 and 5000. For all the simulations, a time step of $\Delta t = 0.01$ has been used. Solutions of lower Re are used as the initial condition for the next higher Re case, thereby reducing computational time significantly.

Figures 1(a) and (b), showing the vertical mid-plane u velocity and the horizontal mid-plane v velocity profiles for $Re = 100$, 400 and 1000, depict an excellent match with the benchmark results even for coarser grids. At high Re it is known that due to the increased relative importance of the non-linear convective term, a range of spatial scales appear in the flow and flow variables admit sharp variation. Thus high accuracy and the superior spectral resolution of the compact schemes are expected to be demonstrated at this range of Re. This can be judged by using a smaller number of grid points than were used in the benchmark solutions. Figures 2(a) and (b) show the results for $Re = 3200$ and 5000. In these cases also, a close match is obtained between the present scheme (on a 41×41 grid) and the benchmark results (on a 256×256 grid). The streamline pattern, shown in Figures 3(a) and (b), clearly resolves three corner vortices at $Re = 3200$ and 5000. Moreover, at $Re = 5000$, all the three corner vortices spread and grow stronger which is also found in the benchmark results.

DOI: 10.1002/fld

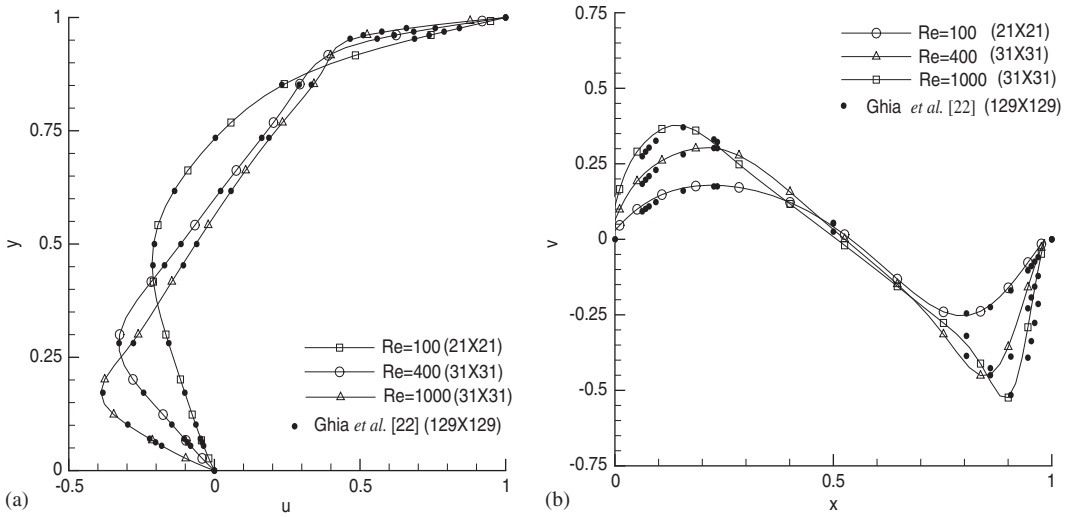

Figure 1. (a) u velocity on the vertical mid-plane; and (b) v velocity on the horizontal mid-plane for $Re \leqslant 1000$.

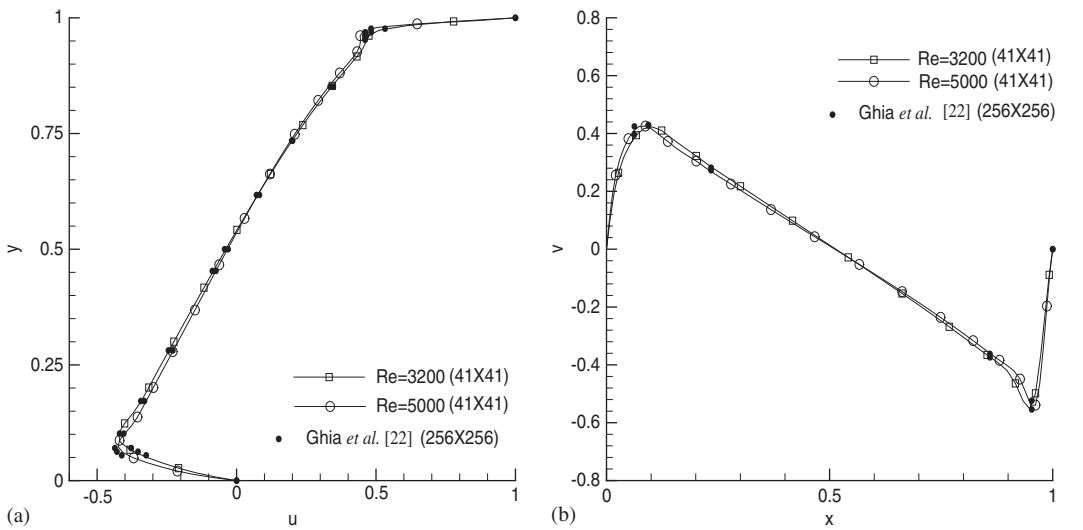

Figure 2. (a) u velocity on the vertical mid-plane; and (b) v velocity on the horizontal mid-plane for $Re = 3200$ and 5000.

A lower order method comprising the standard second-order explicit differencing for all the spatial derivatives retaining the solution algorithm is used to compare the relative CPU time with the present method. As fewer grid points is required to reach the benchmark solution with the present higher order method it takes much lower CPU time (Table I) compared to the lower order

DOI: 10.1002/fld

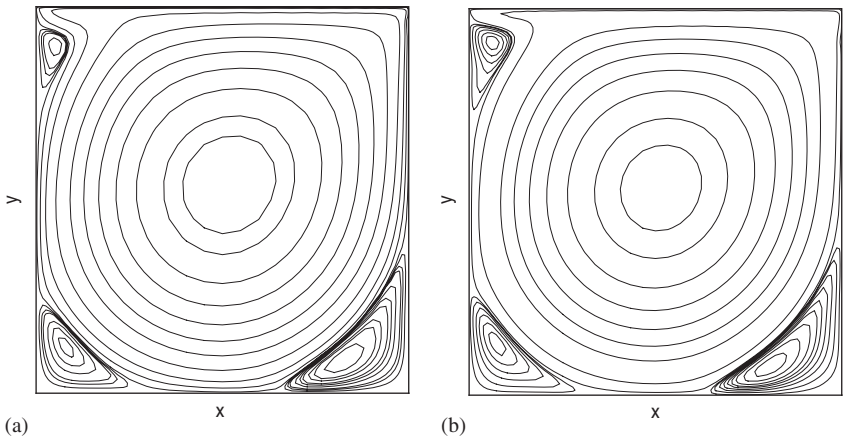

Figure 3. Streamline patters for: (a) $Re = 3200$; and (b) $Re = 5000$.

Table I. Comparison of CPU time taken by the present method and a second-order method.

Re	Present method (s)	Second-order method (s)
100	59	84
400	479	2105
1000	3974	37 618
3200	19 022	57 238

Table II. Perceived order for the driven cavity problem.

Re	u-order	v-order	ψ-order	ω-order
1000	3.731	3.526	3.851	3.477
3200	3.458	3.21	3.641	3.296

method in which a large number of grid points are required to achieve the same. For the second order method, 41×41 grid points are required at $Re = 100$, 101×101 for $Re = 400$ and 129×129 for $Re = 1000$ and 3200 compared to the coarser grids required for the compact schemes (see previous paragraph). The order of accuracy test, described in Section 4.4, has been conducted for the driven cavity problem in the range $100 \leqslant Re \leqslant 3200$. Table II reports the perceived order of accuracy for various solution variables. It is observed that with increase in *Re* accuracy decreases for all the flow variables. As vorticity takes boundary conditions derived from the flow solutions its accuracy is lowest, while the stream function admitting prescribed boundary conditions have the largest accuracy.

DOI: 10.1002/fld

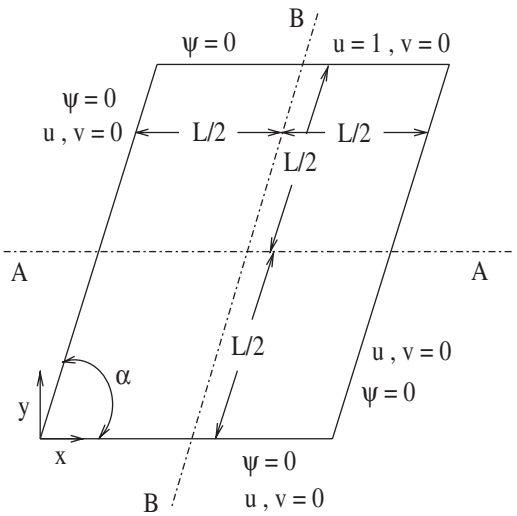

Figure 4. Geometric features of the inclined cavity with boundary conditions.

4.2. Inclined driven cavity

This problem, a variant in non-orthogonal geometry (see Figure 4) of the classical lid-driven cavity problem has been solved for two different inclination of the vertical walls, namely $\alpha = 45°$ and $30°$ at $Re = 100$ and 1000 and compared with Demirdzic *et al.* [23] who used a multi-grid based finite volume method with 320×320 at the finest grid level. In the present work an uniform grid of 51×51 with $\Delta t = 0.01$ has been used.

Figures 5(a) and (b) show the u- and v-velocity profile at vertically inclined mid-plane (plane B–B of Figure 4) and horizontal mid-plane (plane A–A of Figure 4). A close match is obtained with Demirdzic *et al.* [23] using fewer grid points compared to the reported benchmark results. Streamlines for $\alpha = 45°$ (Figure 6) shows that at small Re the main vortex fills almost the whole cavity with a small secondary vortex confined deep in the corner region. With increased Re, the main vortex formed due to the lid velocity weakens and the corner vortex grows into the body of the cavity and is accompanied by the appearance of a third vortex near the bottom corner. Figure 7 shows the flow pattern for $\alpha = 30°$, a case with extremely non-orthogonal geometry. The flow pattern is similar to the previous case with slightly weaker primary and secondary vortices, due to the reduction in mass flow rate accompanying the smaller volume of the cavity. These observations are in good agreement with Demirdzic *et al.* [23]. Table III gives the quantitative comparison of the strength and the location of the vortex centre with Demirdzic *et al.* [23]. It is clear that the location and the strength of the vortices are well resolved in the present study, despite the much coarser grid used, which again confirms the high accuracy and superior resolution capability of compact schemes.

4.3. Viscous flow in a triangular cavity

Flow in a triangular cavity, whose geometric features and boundary conditions along with a typical grid are shown in Figures 8(a) and (b), is solved for $Re \leqslant 1500$. In the present case the cavity being

DOI: 10.1002/fld

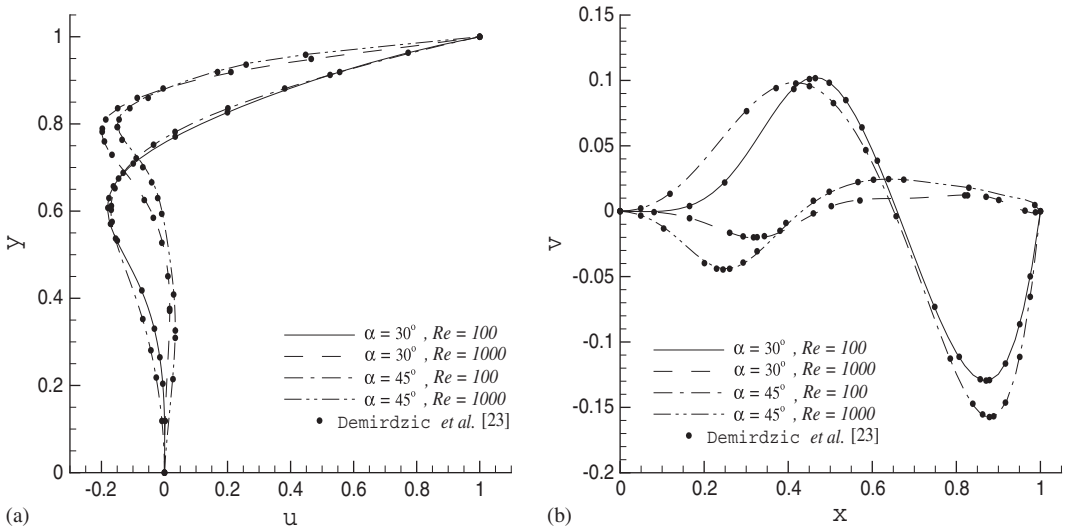

Figure 5. (a) u velocity on the vertically inclined mid-plane; and (b) v velocity on the horizontal mid-plane. Present computations done at 51×51 while 320×320 CVs were used by Demirdzic *et al.* [23].

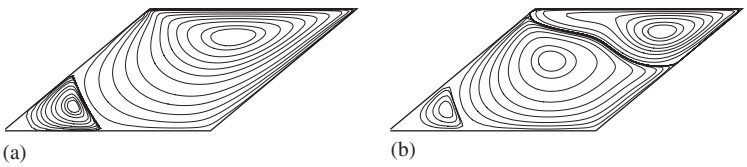

Figure 6. Streamline pattern for $\alpha = 45°$: (a) $Re = 100$; and (b) $Re = 1000$.

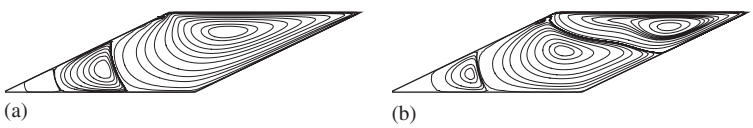

Figure 7. Streamline pattern for $\alpha = 30°$: (a) $Re = 100$; and (b) $Re = 1000$.

an equilateral cavity, $A = \sqrt{3}$, $s = 2$ and $H = 3$. The Reynolds number is based on the characteristic length $H/3$ and reference velocity U, the velocity of the lid, which is consistent with previous works [24–26]. It should be noted that if a side of the cavity is used as the length scale, the actual Re would be increased $2\sqrt{3}$-fold. For all Re, a 40×40 grid has been used here while finer grids of 80×80 and 200×200 were used in References [24, 25], respectively.

Tables IV and V show the detailed characteristics of the primary and secondary eddies, respectively. It can be seen that present results are in good agreement with the earlier studies. The streamline pattern at different Re are shown in Figure 9. A primary and a bottom vortex exist at all Reynolds numbers. However, as Re is increased beyond 500 a upper corner vortex also

DOI: 10.1002/fld

Table III. Minimum and Maximum stream function values in vortex centres and their position, as predicted by the present work (51×51) and Demirdzic *et al.* [23] (320×320).

Re	Source	$\psi_{\min}$, location	$\psi_{\max}$, location
$\alpha = 45°$			
100	Present	-7.031×10^{-2}, (1.111, 0.551)	3.657×10^{-5}, (0.341, 0.141)
100	Demirdzic *et al.* [23]	-7.023×10^{-2}, (1.110, 0.546)	3.683×10^{-5}, (0.339, 0.143)
1000	Present	-5.385×10^{-2}, (1.319, 0.579)	1.013×10^{-2}, (0.790, 0.410)
1000	Demirdzic *et al.* [23]	-5.351×10^{-2}, (1.313, 0.574)	1.004×10^{-2}, (0.777, 0.398)
$\alpha = 30°$			
100	Present	-5.315×10^{-2}, (1.178, 0.380)	5.619×10^{-5}, (0.524, 0.141)
100	Demirdzic *et al.* [23]	-5.313×10^{-2}, (1.166, 0.379)	5.606×10^{-5}, (0.527, 0.143)
1000	Present	-3.902×10^{-2}, (1.450, 0.410)	4.281×10^{-3}, (0.910, 0.260)
1000	Demirdzic *et al.* [23]	-3.856×10^{-2}, (1.458, 0.411)	4.149×10^{-3}, (0.904, 0.255)

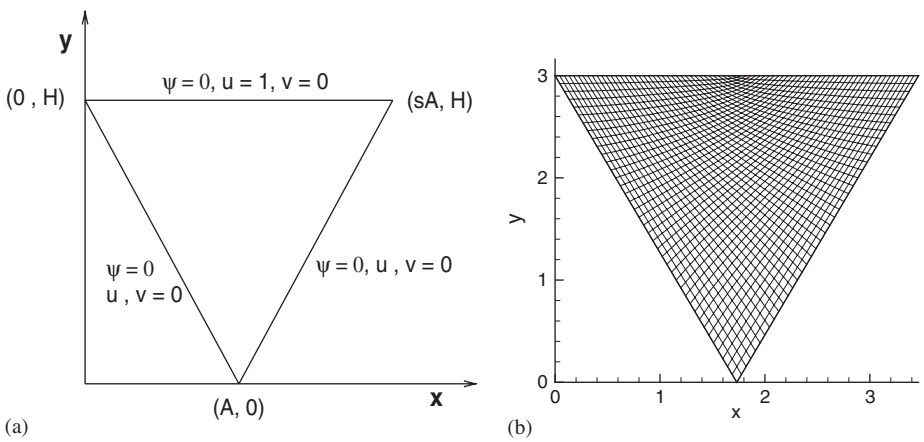

Figure 8. Equilateral triangular cavity: (a) geometric features; and (b) numerical grid.

appears and grows with *Re*. This is also evident from the absolute values of the stream function given in Table V for the upper corner vortex. According to the mean square law, the theoretical value of vorticity at the primary vortex centre is 1.054 for equilateral cavity with side $2\sqrt{3}$. This interior constant vorticity prediction is given by Batchelor [27]. Present numerical results suggest that the stream function value at the centre of the primary eddy, ψ_c, converges to a constant, and its vorticity, ω_c is quite close to 1.054 as $Re > 500$.

4.4. Flow through a constricting channel

Viscous flow in a constricting channel has been used to test the order of accuracy of the present numerical method. A conformal mapping from the physical plane (x, y) to the computational plane

DOI: 10.1002/fld

Table IV. Comparisons of (ψ_c, ω_c) at the centre of the primary eddy, (x_c, y_c) between Li and Tang [24] (80×80), McQuain *et al.* [26] and the present method (40×40).

Re	Source	ψ_c	ω_c	x_c	y_c
	Present	0.237	1.478	2.087	2.446
50	McQuain *et al.* [26]	0.237	1.464	2.078	2.445
	Li and Tang [24]	0.235	1.438	2.100	2.438
	Present	0.248	1.360	2.043	2.347
100	McQuain *et al.* [26]	0.247	1.373	2.061	2.355
	Li and Tang [24]	0.244	1.264	2.100	2.363
	Present	0.260	1.246	1.954	2.269
200	McQuain *et al.* [26]	0.260	1.272	1.940	2.280
	Li and Tang [24]	0.262	1.156	1.905	2.250
	Present	0.270	1.160	1.865	2.195
500	McQuain *et al.* [26]	0.269	1.250	1.905	2.265
	Li and Tang [24]	0.278	1.124	1.840	2.213
	Present	0.271	1.145	1.865	2.195
600	Li and Tang [24]	0.280	1.110	1.862	2.175
	Present	0.267	1.093	1.865	2.195
1000	Li and Tang [24]	0.279	1.048	1.840	2.138
	Present	0.262	1.053	1.821	2.159
1200	Li and Tang [24]	0.278	1.024	1.840	2.138
	Present	0.256	1.016	1.821	2.159
1500	Li and Tang [24]	0.277	0.998	1.840	2.138

Table V. The feature of the eddies in the triangular cavity at high Reynolds number.

	Bottom eddy	Upper corner eddy
Re	ψ, ω, location	ψ, ω, location
600	(a) -0.0116, -0.5851, $(1.509, 1.061)$	-0.0002, -0.151, $(0.444, 2.514)$
	(b) -0.0115, -0.5672, $(1.559, 0.975)$	-0.0002, -0.1451, $(0.390, 2.475)$
1000	(a) -0.0123, -0.6585, $(1.509, 1.061)$	-0.00331, -0.5371, $(0.488, 2.634)$
	(b) -0.0125, -0.6779, $(1.537, 0.938)$	-0.0024, -0.5608, $(0.455, 2.588)$
1200	(a) -0.0127, -0.5682, $(1.554, 0.996)$	-0.00411, -0.409, $(0.488, 2.635)$
	(b) -0.0126, -0.6507, $(1.559, 0.900)$	-0.0033, -0.5081, $(0.455, 2.588)$
1500	(a) -0.01419, -0.5839, $(1.554, 0.996)$	-0.0051, -0.6034, $(0.444, 2.706)$
	(b) -0.0125, -0.7275, $(1.537, 0.863)$	-0.0045, -0.6393, $(0.433, 2.625)$

(a) Present (40×40), (b) Li and Tang [24] (80×80).

(ξ, η) [28] has been effected to obtain a constricting channel geometry

$$x = A\xi + \frac{B}{H}[\xi \sinh(2\xi) - \eta \sinh(2\eta)], \quad y = A\eta + \frac{B}{H}[\eta \sinh(2\xi) + \xi \sinh(2\eta)] \tag{18}$$

where $H = \cosh(2\xi) + \cosh(2\eta)$ and A, B are constants. Figure 10(a) shows the flow geometry along with boundary conditions. The Jacobian of the transformation becomes zero at a point of co-ordinate singularity, $(\xi_0, \eta_0) = (0.562101, 1.049059)$, leading to the possibility of construction of a symmetric channel with an arbitrarily sharp corner. The computational domain is given by the region $-\infty < \xi < \infty$ and $-\lambda < \eta < \lambda$, where $\lambda < \eta_0$. As the value of λ approaches η_0, the domain

DOI: 10.1002/fld

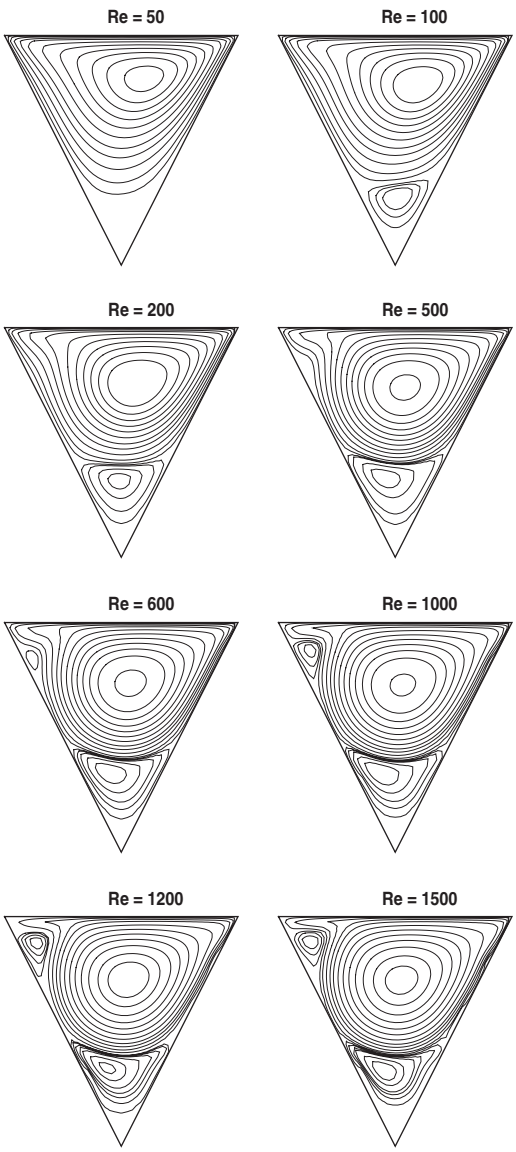

Figure 9. Development of primary and secondary eddies for $50 \leqslant Re \leqslant 1500$.

of flow has an increasingly sharp corner. If it is supposed that the diameter of the tube is $2a$ far upstream and $2b$ far downstream; then A and B are given as

$$A = \frac{a+b}{2\lambda}, \quad B = \frac{b-a}{2\lambda}$$

Two values of λ has been tested in the present computation with $a = 1$, $b = 0.5$. While $\lambda = 0.6$ represents a smooth constriction (Figure 10(b)), while $\lambda = 0.8$ represents a smooth constriction

DOI: 10.1002/fld

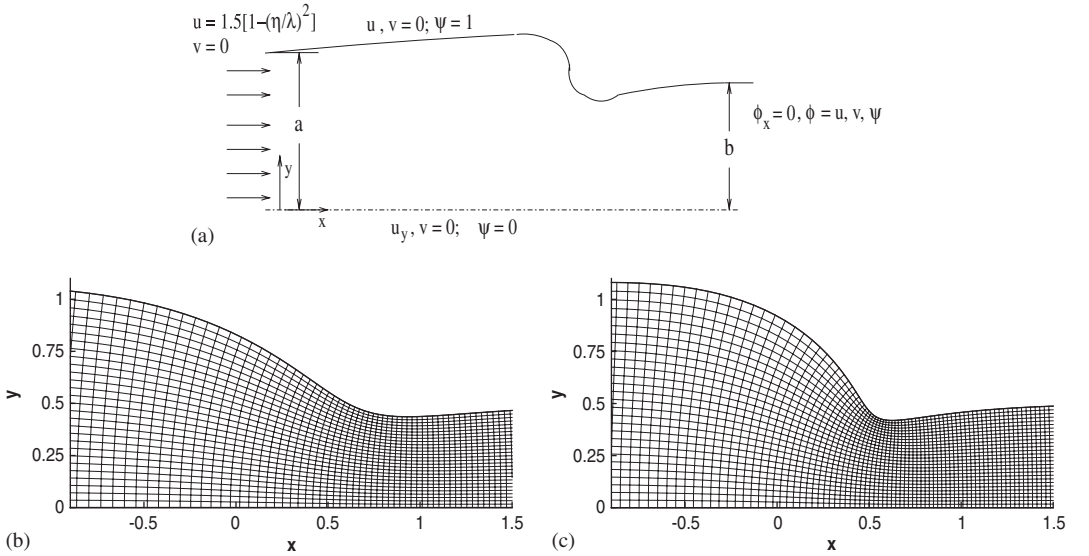

Figure 10. (a) Flow geometry with boundary conditions; close view of the grid near the constriction for; (b) $\lambda = 0.6$; and (c) $\lambda = 0.8$.

but with an intrusive bulge at the mouth of the inner channel (see Figure 10(c)). The numerical solution has been obtained for three levels of grids namely, a coarse grid of 32×8, a medium grid of 64×16 and a fine grid of 128×32 in ξ and η directions respectively. The range of ξ is chosen to be $-2<\xi<3$, with the critical point ξ_0 being approximately at the midpoint. This leads to x approximately in the range $2a/\lambda<x<3b/\lambda$ using Equation (18).

If ϕ_C, ϕ_M and ϕ_F are the numerical solutions at a common location in the coarse, middle and the fine grids, respectively, and if ϕ is the exact solution at that point then the perceived order of accuracy α, can be written as

$$\phi - \phi_F = Kh^\alpha, \quad \phi - \phi_M = K(2h)^\alpha, \quad \phi - \phi_C = K(4h)^\alpha$$

where K is a constant and h is the grid spacing at the finest level. Eliminating ϕ and K gives

$$\frac{\phi_M - \phi_C}{\phi_F - \phi_M} \approx 2^\alpha$$

from which α can be found. In the present computation, the root mean square error has been used between two successive grid levels to evaluate α. This is given as

$$\frac{\sqrt{\sum\sum(\phi_M - \phi_C)^2}}{\sqrt{\sum\sum(\phi_F - \phi_M)^2}} \approx 2^\alpha \Longrightarrow \frac{R_M}{R_F} = 2^\alpha \Longrightarrow \alpha = \frac{\log(R_M/R_F)}{\log 2}$$

where summation implies over all points with same location for the three different grids. Three different Reynolds numbers namely, $Re = 50$, 100 and 250 have been used for both $\lambda = 0.6$ and 0.8. In Table VI, the computed order of accuracy for all variables are shown. In all the cases the order of accuracy is greater than 3, and close to 4. As Reynolds number increases, however, the

DOI: 10.1002/fld

Table VI. Perceived order for $\lambda = 0.6$ and 0.8.

λ	Re	u-order	v-order	ψ-order	ω-order
	50	4.021	4.587	4.889	3.742
0.6	100	3.981	3.847	4.455	3.704
	250	3.645	3.513	3.821	3.41
	50	4.351	4.274	4.876	3.85
0.8	100	3.787	3.521	4.13	3.421
	250	3.534	3.258	3.658	3.121

order of accuracy for all the variables deteriorates. For $\lambda = 0.8$, the order of accuracy deteriorates somewhat more but remains above 3. For all cases, ψ gives the highest numerical order of accuracy while ω gives the lowest. This is presumably because solutions of higher order quantities (e.g. vorticity depends on the spatial derivatives of velocity, which in turn depend on derivatives of stream function) tend to have more numerical error.

5. CONCLUSIONS

A high-order accurate method using the ψ–ω formulation is developed for two-dimensional incompressible steady viscous flows. Implicit time integration facilitates reaching steady state with less computations. The use of higher order optimized compact schemes provide excellent accuracy and resolution with fewer grid points than that of benchmark results. Tests on highly non-uniform and curvilinear grids show that the spatial order of accuracy of the numerical solutions remains above 3 in all cases, and approaches 4 for low Reynolds numbers.

REFERENCES

1. Lotstedt P, Nilsson J, Bruger A, Gustafsson B. High order accurate solution of the incompressible Navier–Stokes equations. *Journal of Computational Physics* 2005; **203**:49–71.
2. Bhaganagar K, Rempfer D, LumleLele D. Direct numerical simulation of spatial transition to turbulence using fourth-order vertical velocity second-order vertical vorticity formulation. *Journal of Computational Physics* 2002; **180**:200–228.
3. Henshaw WD. A fourth-order accurate method for the incompressible Navier–Stokes equations on overlapping grids. *Journal of Computational Physics* 1994; **113**:13–25.
4. Li M, Tang T, Fornberg B. A compact fourth-order finite difference scheme for the steady incompressible Navier–Stokes equations. *International Journal for Numerical Methods in Fluids* 1995; **20**:1137–1151.
5. Morinishi Y, Lund TS, Vasilyev OV, Moin P. Fully conservative higher order finite difference schemes for incompressible flow. *Journal of Computational Physics* 1998; **143**:90–124.
6. Nagarajan S, Lele SK, Ferziger JH. A robust high-order compact method for large eddy simulation. *Journal of Computational Physics* 2003; **191**:392–419.
7. Strikwerda JC. High-order-accurate schemes for incompressible viscous flow. *International Journal for Numerical Methods in Fluids* 1997; **24**:715–734.
8. Tam CKW, Webb JC. Dispersion-relation-preserving finite difference schemes for computational acoustics. *Journal of Computational Physics* 1993; **107**:262–281.
9. Zingg DW, Lomax H, Jurgens H. High accuracy finite difference schemes for linear wave propagation. *SIAM Journal on Scientific and Statistical Computations* 1996; **17**:328–346.
10. Li Y. Wavenumber-extended high-order upwind-biased finite-difference schemes for convective scalar transport. *Journal of Computational Physics* 1997; **133**:235–255.

DOI: 10.1002/fld

11. Kawamura T, Takami H, Kuwahara K. New higher order upwind scheme for incompressible Navier–Stokes equations. *Fluid Dynamic Research* 1985; **1**:145–162.
12. Lele SK. Compact finite difference schemes with spectral-like resolution. *Journal of Computational Physics* 1992; **103**:16–42.
13. Hixon R, Turkel E. Compact implicit Maccormack-type schemes with high accuracy. *Journal of Computational Physics* 2000; **158**:51–70.
14. Zhong X. High-order finite-difference schemes for numerical simulation of hypersonic boundary-layer transition. *Journal of Computational Physics* 1998; **144**:662–709.
15. Chu PC, Fan C. A three-point sixth-order non-uniform combined compact difference scheme. *Journal of Computational Physics* 1999; **148**:663–674.
16. De AK, Eswaran V. Analysis of a new high resolution upwind compact scheme. *Journal of Computational Physics* 2006, in press.
17. Sotiropoulos F, Abdallah S. The discrete continuity equation in primitive variable solutions of incompressible flow. *Journal of Computational Physics* 1991; **95**:212–227.
18. Petersson NA. Stability of pressure boundary conditions for Stokes and Navier–Stokes equations. *Journal of Computational Physics* 2001; **172**:40–70.
19. Wu XH, Wu JZ, Wu JM. Effective vorticity–velocity formulations for three-dimensional incompressible viscous flows. *Journal of Computational Physics* 1995; **122**:68–82.
20. Quartapelle L, Napolitano M, Pascazio G. A review of vorticity conditions in the numerical solution of the ω–ψ equations. *Computers and Fluids* 1999; **28**:139–185.
21. van der Vorst HA. A fast and smoothly convergence variant of bi-cg for the solution of nonsymmetric linear systems. *SIAM Journal on Scientific and Statistical Computations* 1992; **13**:631–644.
22. Shin CT, Ghia U, Ghia KN. Higher-order-accurate schemes for viscous flows. *Journal of Computational Physics* 1982; **48**:387–411.
23. Demirdzic I, Peric M, Lilek Z. Fluid flow and heat transfer test problems for non-orthogonal grids: Benchmark solutions. *International Journal for Numerical Methods in Fluids* 1992; **15**:329–354.
24. Li M, Tang T. Steady viscous flow in a triangular cavity by efficient numerical techniques. *Computers and Mathematics with Applications* 1996; **31**:55–65.
25. Wang CY, Ribbens CJ, Watson LT. Steady viscous flow in a triangular cavity. *Journal of Computational Physics* 1994; **112**:173–181.
26. McQuain WD, Ribbens CJ, Wang CY, Watson LT. Steady viscous flow in a trapezoidal cavity. *Computers and Fluids* 1994; **23**:613–626.
27. Batchelor GK. On steady laminar flow with closed streamlines at large Reynolds number. *Journal of Fluid Mechanics* 1956; **1**:177–190.
28. Hunt R, Mancera PF, De A. Fourth-order method for solving the Navier–Stokes equations in a constricting channel. *International Journal for Numerical Methods in Fluids* 1997; **25**:1119–1135.

DOI: 10.1002/fld